HHS Public Access

Author manuscript

Pharm Res. Author manuscript; available in PMC 2021 December 10.

Published in final edited form as:

Pharm Res. ; 37(10): 199. doi:10.1007/s11095-020-02923-8.

CFD Guided Optimization of Nose-to-Lung Aerosol Delivery in Adults: Effects of Inhalation Waveforms and Synchronized Aerosol Delivery

Rabijit Dutta[1], **Benjamin Spence**[1], **Xiangyin Wei**[2], **Sneha Dhapare**[2], **Michael Hindle**[2], **P. Worth Longest**[1,2,*]

[1]Department of Mechanical and Nuclear Engineering, Virginia Commonwealth University, Richmond, VA

[2]Department of Pharmaceutics, Virginia Commonwealth University, Richmond, VA

Abstract

Purpose.—The objective of this study was to optimize nose-to-lung aerosol delivery in an adult upper airway model using computational fluid dynamics (CFD) simulations in order to guide subsequent human subject aerosol delivery experiments.

Methods.—A CFD model was developed that included a new high-flow nasal cannula (HFNC) and pharmaceutical aerosol delivery unit, nasal cannula interface, and adult upper airway geometry. Aerosol deposition predictions in the system were validated with existing and new experimental results. The validated CFD model was then used to explore aerosol delivery parameters related to synchronizing aerosol generation with inhalation and inhalation flow rate.

Results.—The low volume of the new HFNC unit minimized aerosol transit time (0.2 s) and aerosol bolus spread (0.1 s) enabling effective synchronization of aerosol generation with inhalation. For aerosol delivery correctly synchronized with inhalation, a small particle excipient-enhanced growth delivery strategy reduced nasal cannula and nasal depositional losses each by an order of magnitude and enabled ~80% of the nebulized dose to reach the lungs. Surprisingly, nasal deposition was not sensitive to inhalation flow rate due to use of a nasal cannula interface with co-flow inhaled air and the small initial particle size.

Conclusions.—The combination of correct aerosol synchronization and small particle size enabled high efficiency nose-to-lung aerosol delivery in adults, which was not sensitive to inhalation flow rate.

Keywords

Trans-nasal aerosol delivery; high flow nasal cannula; pharmaceutical aerosols; high-efficiency aerosol delivery; nebulized aerosol

[*]**Author Contact Information:** P. Worth Longest, PhD (Corresponding author), Virginia Commonwealth University, 401 West Main Street, P.O. Box 843015, Richmond, VA 23284-3015, Phone: (804)-827-7023, Fax: (804)-827-7030, pwlongest@vcu.edu.

DISCLOSURES

Virginia Commonwealth University is currently pursuing patent protection of EEG aerosol delivery, mixer-heater systems and patient interfaces, which if licensed, may provide a future financial interest to the authors.

INTRODUCTION

The administration of inhaled pharmaceutical aerosols through the nose and to the lungs (i.e., nose-to-lung or trans-nasal aerosol delivery) may provide a beneficial and convenient alternative to oral inhalation in a number of situations (1–4). Applications where nose-to-lung administration may be advantageous include the simultaneous delivery of aerosol and ventilation gas during non-invasive ventilation (NIV) (4, 5); delivery of high dose or rapidly absorbed medications (6–8); treatment of the nasal and lung airways simultaneously (9, 10); and delivering therapeutics that may have improved efficacy with extended delivery periods, such as hypertonic saline (11) or beta-lactam antibiotics (12, 13). Trans-nasal aerosol delivery is also useful for infants and children that are too young to use an inhaler as well as for sedated or sleeping patients (4, 7, 14, 15).

Of the potential nose-to-lung applications, aerosol delivery concurrent with high-flow nasal cannula (HFNC) ventilation therapy is especially challenging (4, 16–18). HFNC therapy is a form of ventilation support in which a continuous and steady-state gas flow of air or blended oxygen is delivered through a loose-fitting nasal cannula (19, 20). Heating and humidification of the gas allow flow rates of approximately 15 L/min (LPM) and higher for adults to be comfortably delivered. A gap between the nasal cannula and nostrils enables room for exhaled gas to escape as well as additional inhaled air to enter. By delivering the gas continually, HFNC supports respiration through washing out CO_2 in the upper airways, reducing the work of breathing, and potentially providing airway pressure support (21). However, the associated high gas flow rates, narrow nasal cannula interface, and uncontrolled environmental gas losses are challenges for the simultaneous delivery of therapeutic aerosols (22, 23).

While nose-to-lung aerosol delivery may be convenient and beneficial, aerosol delivery efficiency via the nose to the lungs is very low and especially poor for aerosol administration simultaneous with HFNC therapy. Based on *in vitro* studies with commercial components evaluated under adult conditions, estimated drug delivery through a nasal cannula interface is typically less than approximately 30% of the nebulized dose (1, 16, 24, 25). Increasing the delivery flow rate to a value of 20 LPM or higher typically reduces delivery efficiency to 3% or less of the nebulized dose (16, 17). For example, Perry et al. (16) considered nebulized aerosol delivery through an adult nasal cannula at multiple flow rates and reported an ex-cannula dose of 0.4% and below at flow rates of 20 LPM and above. Including a realistic nasal geometry also significantly reduces the estimated lung dose compared with assessing dose delivered at the exit of a nasal cannula or face mask (23, 24).

Low lung delivery efficiencies reported with *in vitro* studies during nose-to-lung administration are consistent with established *in vivo* experiments of aerosol delivery during all forms of NIV (4, 5, 26–28). Considering aerosol administration during HFNC therapy, Dugernier et al. (29) recently conducted human *in vivo* studies of lung delivery efficiency using a radiolabeled aerosol. At a standard HFNC flow rate of 30 LPM, <5% of the loaded dose in a mesh nebulizer reached the lungs (29).

Despite low lung delivery efficiency during nose-to-lung aerosol administration, clinical efficacy is reported for inhaled bronchodilators when administered with a mask (4, 5, 27) or nasal cannula (30). Bronchodilators like albuterol sulfate are highly potent such that poor delivery efficiency may be acceptable in most patient populations. However, high nasal depositional loss is likely associated with high variability in the lung delivered dose (31, 32). For an individual patient, physicians often do not know how much of the drug is lost in the extrathoracic airways and swallowed and how much reaches the lungs (18). Improved lung delivery efficiency will waste less medication, reduce side effects associated with dose ingestion, and reduce intersubject variability. These improvements are expected to be necessary if trans-nasal delivery is extended beyond bronchodilator administration. Medications that likely require improved administration through increased lung delivery efficiency and delivery rate include inhaled antibiotics, vasodilators, next generation anti-inflammatory medications, antivirals, and biologicals (8, 33–35).

To improve aerosol delivery during HFNC therapy, or for stand-alone high efficiency aerosol administration, a large-volume mixer-heater device was previously developed and tested (23, 36). This device included a large-volume mixing region that received the aerosol from the mesh nebulizer, combined the aerosol with ventilation gas and held the aerosol with low depositional loss during periods of exhalation. An attached heating section in the form of a narrow channel was used to reduce aerosol size as well as provide heat and humidity to the inhaled air (36). Under steady state operating conditions with a HFNC flow rate of 30 LPM, Golshahi et al. (23) demonstrated that up to 80% of the nebulized dose could be delivered through a streamlined nasal cannula interface (37, 38) and adult *in vitro* nasal replica to a tracheal filter (23). The large volume mixing region allowed for continuous operation of the nebulizer during cyclic inhalation, which maintained a high drug delivery rate. However, deep nasal inhalation with a tidal volume of approximately 900 ml was required to empty the mixing chamber and maintain high efficiency nose-to-lung delivery of the aerosol (22, 39).

For cases in which deep nasal inhalation may not be possible, Spence et al. (13) recently developed a simplified mixer-heater design with a post-nebulizer volume of <150 ml. This device is intended for efficient aerosol delivery during HFNC therapy or to serve as a stand-alone nebulized aerosol delivery platform. A unique feature of the small-volume mixer-heater is the use of separate humidity and drug nebulizers. This dual nebulizer design allows for the administration of both HFNC therapy and high efficiency aerosol delivery in one platform. For HFNC administration, the humidity nebulizer is operated continually and intended to administer isotonic or hypertonic saline. For on-demand periods of pharmaceutical aerosol administration, the drug nebulizer is synchronized to actuate during a portion of the inhalation cycle. The humidity nebulizer is turned off during the time that the drug nebulizer is actuated, resulting in an alternating pattern in which one nebulizer is always actuated. Based on the study of Spence et al. (13), the small-volume mixer-heater produced minimal depositional drug loss (approximately 5%) and an approximately 1 μm aerosol during steady state operation at a HFNC gas flow rate of 30 LPM. Outlet temperature and relative humidity (RH) were also acceptable for direct HFNC administration. However, aerosol delivery synchronized with inhalation has not been tested in this device.

The small-volume mixer-heater (13) is currently in development for human subject testing of lung delivery efficiency with a small particle aerosol. Design factors that are currently fixed include the mixer-heater geometry as proposed by Spence et al. (13), a 20 to 30 LPM ventilation gas flow rate to be consistent with HFNC therapy, and a 1 to 1.5 second drug nebulization period with each inhalation to maintain a high drug output. Two factors that will have a large impact on the lung delivery fraction are subject inhalation flow waveform and synchronization of drug nebulization with the inhalation waveform. Considering the breathing waveform, efficient lung delivery occurs when the inhalation flow rate exceeds the HFNC gas flow rate. However, if the peak inhalation flow rate is too high, excessive impaction loss of the aerosol will occur. Defining a range of acceptable inhalation waveforms will help to ensure maximum lung delivery in the human subject trials. If inhalation guidance is needed, as with the AERx (Aradigm Corp.) (40) or I-neb (Philips Respironics) (41) inhalers, a range of acceptable breathing waveforms can be programmed into the inhalation guidance and feedback system.

Considering synchronization of aerosol delivery, there will be a delay between the time point of nebulization and when the aerosol reaches the subject. Moreover, the aerosol bolus will spread over time in a difficult to predict manner as it moves through the mixer-heater, tubing and extrathoracic airways. Understanding this delay and bolus spreading can be used to select a nebulization actuation procedure that maximizes lung delivery efficiency.

A key component of this study is the application of the excipient enhanced growth (EEG) aerosol delivery strategy (42–45). In this approach, relatively small particles [mass median aerodynamic diameter (MMAD) ≤ 1.5 μm] are inhaled, and each particle contains a combination of the delivered therapeutic and a hygroscopic excipient. The small initial particle size enables high efficiency delivery of the aerosol (23, 46–48). Once inside the airways, the hygroscopic excipient absorbs the naturally occurring humidity turning the particles into growing droplets and fostering deposition (23, 45, 49–51). Without hygroscopic size increase, a large portion of the small particle aerosol would likely be exhaled (if a breath hold period is not included) (52). The type and amount of excipient, initial size and inhalation flow rate can all be used to control the growth rate and potentially target the region of aerosol delivery (45, 49–51).

The objective of this study is to understand and optimize nose-to-lung aerosol delivery in an adult upper airway model considering the effects of different inhalation flow rates and aerosol generation synchronization parameters. In contrast with previous studies evaluating aerosol delivery with a large-volume mixer-heater, the current study focuses on a small-volume device, which better enables synchronized aerosol delivery of the pharmaceutical aerosol with inhalation. Furthermore, the current study is the first to use CFD simulations to analyze the timing of aerosol delivery with inhalation and determine the optimal delivery window as well as the effects of elevated inhalation flow rates. A CFD model of aerosol transport, growth, and deposition is first verified and further validated in comparison to *in vitro* experimental data. Transient CFD model predictions are then used to visualize and understand difficult to capture metrics such as the time delay and spread of the aerosol bolus. The information regarding aerosol spread and delay are used along with transient CFD simulations of nose-to-lung delivery to understand the effects of synchronizing the

drug aerosol delivery with nasal inhalation flow. Steady state predictions of aerosol transport and depositional loss are used to estimate required inhalation flow ranges to achieve a targeted lung delivery of 80% of the nebulized dose. These findings will help to determine optimal *in vivo* testing conditions including correct timing of nebulization actuation and if inhalation guidance is needed in order to achieve a lung delivery efficiency of 80% or higher of the nebulized dose.

MATERIALS AND METHODS

In Vitro Study

Experimental Setup—An *in vitro* experimental study was conducted to validate the transient CFD model for EEG delivery during a deep nasal inhalation waveform in terms of regional device deposition and tracheal filter dose (Figure 1). The experimental setup consisted of a small-volume mixer-heater device, a nasal cannula interface, an adult nose-mouth-throat (NMT) geometry and a breathing simulator. The mixer-heater combined the nebulized drug with the HFNC gas and reduced the aerosol size by evaporation, thereby producing micrometer-sized EEG particles. At the inlet of the mixer-heater, HFNC gas was introduced at a steady flow rate of 30 L/min. The drug nebulizer was filled with 0.25% w/v albuterol sulfate (AS) and 0.25% w/v sodium chloride (NaCl) in water (0.5% w/v total solute concentration) and the humidity nebulizer was filled with isotonic saline (0.9% w/v NaCl in water). The drug nebulizer was actuated for a 1.5 s duration by the mixer-heater control system synchronized to deliver the aerosol during a 2.5 s inhalation cycle. To complete the 7.5 s breathing cycle employed in this study, the humidity nebulizer was then actuated for 6 seconds to humidify the HFNC gas. The mixer-heater control unit contained a pressure sensor which recorded the breathing profile and determined the *start of inhalation*. The drug nebulizer was actuated at a separate *start of nebulization* time, which occurred slightly after the sensed *start of inhalation*. The reason for this delay was to allow the inhalation flow rate to be greater than the constant HFNC flow rate at the time the aerosol reached the nostrils. The control unit also regulated the heating element of the mixer-heater to provide outlet gas thermodynamic conditions of 32±2°C and RH >30% (13).

Smooth plastic tubing with an approximate inner diameter of 10 mm connected the mixer-heater to a commercial Optiflow Nasal Cannula MR850 (Fisher & Paykel, Irvine, CA). The cannula employed medium size (OPT544) prongs, which were inserted into the nostrils of an adult NMT geometry. The NMT geometry employed in this study was the “Open” model described by Walenga et al. (53), and has been used in multiple previous *in vitro* and CFD studies (23, 32, 53, 54). The particles exiting the NMT geometry were collected on a low-resistance respiratory filter (PulmoGuard II™, Quest Medical, North Easton, MA, USA).

A breathing simulator (ASL 5000, Ingmar Medical, Pittsburgh, Pennsylvania) was attached to the exit of the tracheal respiratory filter to produce a deep nasal inhalation and exhalation profile during aerosol generation. The details of the breathing waveform include an inhalation period of 2.5 s, a 1:2 inhalation:exhalation ratio, a tidal volume of 1750 ml, mean and peak inspiratory flow rates of 42 and 66 LPM, respectively, and a sinusoidal shape. These breathing instructions are intended to be representative of a patient that is

instructed to “breathe deeply through the nose with a closed mouth” during the period of pharmaceutical aerosol administration. The prescribed deep nasal inhalation waveform was based on the study of Franca et al. (55) for bi-level noninvasive ventilation. Compared with ICRP (56) data, this waveform is reasonable for both male and female subjects with moderately elevated breathing effort.

Particle Sizing and Drug Deposition—Aerodynamic particle sizing experiments were performed using the Andersen Cascade Impactor (ACI; Copley Scientific, Nottingham, United Kingdom) operating at 30 LPM and housed in an environmental chamber (Espec, Hudsonville, MI), which was set to a temperature of 35°C and relative humidity (RH) of 99% to minimize effects of evaporation/condensation size changes during measurements. To determine the size distribution of the aerosol, the outlet of the mixer-heater operated at 30 LPM was positioned in front of the ACI, which was oriented horizontally.

Regional drug deposition of the nebulized aerosol was determined in separate experiments (n = 3) with the mixer-heater connected to the smooth tubing (Tubing 1), cannula tubing (Tubing 2), nasal cannula, NMT model and respiratory filter positioned at the start of the trachea (Figure 1). Depositional areas of interest were the mixer-heater, tubings, nasal cannula interface, nasal model, and expected lung dose as estimated by drug capture on the respiratory filter. Drug deposited on the mixer heater components, cannula, and the nose-mouth-throat (NMT) model and respiratory filter (or ACI plates for aerosol size distribution) was recovered and analyzed using a validated isocratic high-performance liquid chromatography (HPLC) method (57). Briefly, this analysis involved washing each component with known volumes of deionized water such that the drug concentration of the sample fell within the 0.5–16 μg/mL range of the calibration standards. The measured drug concentrations in the collected samples were then determined using quantitative HPLC analysis. The nominal dose of drug nebulized was determined by subtraction of the amount of drug remaining in the nebulizer reservoir (determined by quantitative HPLC) following each experiment from the initial mass of drug loaded into the nebulizer (determined from the known volume added and quantitative HPLC determination of its concentration). Regional drug mass deposition on the system components was calculated from the product of the measured drug concentration and the wash volume and expressed as a percentage of the nominal nebulized dose. The total recovered dose was reported as the sum of drug recovered from all deposition sites expressed as a percentage of the nominal nebulized dose. Initial experimental runs utilizing a continuous pull of air through the model, instead of the lung simulator, indicated virtually 100% recovery of drug. Therefore, in subsequent experimental runs with the lung simulator, exhaled dosages were reasonably approximated by the percentage of nebulized drug not recovered.

CFD Methodology

Geometry—The numerical geometry closely resembled the experimental setup, and was divided into two separate CFD systems: the ‘mixer-heater’ (System 1) and the ‘cannula/NMT’ (System 2) as shown in Figure 2. System 1 consists of the drug and humidity nebulizers, mixer-heater, and Tubing 1; whereas System 2 consists of the cannula interface (Tubing 2+nasal cannula) and the NMT model. Transient CFD simulations in the mixer-

heater (System 1) aid understanding of the effect of bolus spread over time and delay of the drug particles leaving the mixer-heater. The information regarding the temporal spread and the time delay in combination with the measured polydisperse size distribution of the EEG aerosols were used to specify the parameters of aerosol entering the cannula/NMT (System 2).

Solution Approach—A CFD model was implemented in a commercially available package, ANSYS FLUENT 19.1 (ANSYS Inc.), in conjunction with multiple user-defined routines. To simulate the composite flow field consisting of laminar, transitional and fully turbulent conditions, a low-Reynolds number (LRN) k-ω model was selected. The variable temperature and RH fields were resolved by solving coupled equations for heat and mass transfer (58, 59). Lagrangian transport equations were employed to model the particle trajectories, including the hygroscopic size change (44, 54). The effect of turbulent dispersion on the particle trajectories was modeled using a random walk approach (60, 61).

All transport equations were discretized to be second order accurate in space. A second order upwind scheme was used to interpolate values from cell centers to nodes for all terms except for diffusion, which was discretized using a central difference scheme. Double precision computation was used for all calculations to improve accuracy, which is particularly important in regions of rapid change for flow, heat, and mass transport. The pressure-velocity coupling was modeled using the SIMPLEC algorithm, and the gradient discretization was modeled using the least-square cell-based scheme. Flow field convergence was achieved when the global mass-residual was reduced by four orders of magnitude and the residual rates of reduction for mass, momentum, and turbulence transport equations approached the numerical precision limit.

CFD Model Extensions—The LRN k-ω model, like most two-equation Reynolds-Averaged Navier Stokes (RANS) models, assumes isotropic turbulence in the near-wall region, resulting in over-prediction of microparticle deposition. Based on work by Matida et al. (61) and Wang and James (62), Longest and Xi (63) developed FLUENT user-defined functions (UDF) to introduce the anisotropic velocity fluctuations in the continuous phase solution. Furthermore, Longest and Xi (63) implemented UDFs to model particle–wall hydrodynamic interactions (64) by damping the wall-normal velocity in the near-wall region on the scale of individual particle diameters. More details on these UDFs have been reported in previous studies from our group (63, 65). The main control parameter used in the velocity damping UDF is the near-wall (NW) limit (65) such that the wall-normal velocity is damped if a particle is below this height. The NW limit is set to 1 μm in this study based on the recommendations suggested by Bass and Longest (65).

The hygroscopic size change of the particles due to evaporation and condensation was modeled using a UDF. This model accounts for heat and mass transfer relations for multi-component hygroscopic droplets and includes the Kelvin effect, the effects of droplet surface vapor change due to temperature, and the hygroscopicity of the drugs and excipient (44, 54). Interaction between evaporating and condensing droplets with the continuous phase can be modeled by considering either one-way or two-way coupling effects. In one-way coupling, evolution of droplets does not affect the heat and mass transfer in the continuous phase,

while two-way coupling considers the effect of the droplets on the continuous phase. Mass and energy sources or sinks in the continuous phase as a result of two-way coupling were modeled using UDFs (36, 44, 51).

CFD Boundary Conditions—The CFD boundary conditions were chosen to approximate the concurrent *in vitro* experiments. In the cannula/NMT system, a velocity inlet boundary condition with a fully developed parabolic profile was employed at the delivery tube, which matched the HFNC flow rate of 30 LPM. Further, transient velocity inlet conditions were used at the left and the right nostrils in the gap between cannula and airway walls to model the experimental deep nasal inhalation profile. Based on preliminary resistance calculations, it was estimated that 60% of environmentally inhaled flow enters through the left nostril, whereas the remaining 40% enters through the right nostril. A constant pressure boundary condition was used at the NMT outlet to model the respiratory filter. To prevent recirculating flow from crossing the pressure outlet, which reduces CFD solution quality, a numerical extension with a length of five times the outlet diameter was added. The turbulence conditions at the boundaries for the LRN k-ω model were specified using the hydraulic diameter and turbulence intensity. At the tubing inlet, turbulence intensity was set to 0.0001% (53). Further, turbulence intensity at the nostril inlets was prescribed as 1%. Changing the turbulence intensity to 5% both at the tubing inlet and the nostril inlets showed a negligible influence on the deposition fractions. The temperature and the RH at the tubing inlet were set to 32 °C and 30% to match the conditions at the mixer-heater outlet, while the temperature and RH were set to 22 °C and 50% at the nostrils to match the room ambient conditions. The temperature and RH at the walls of the mixer-heater, tubing and cannula were set to 25 °C and dry conditions (0% RH), respectively.

In addition to transient CFD simulations through the cannula/NMT system, steady state simulations were conducted through the NMT geometry connected to an upper tracheobronchial (TB) airway geometry of an adult (Model D). The temperature and RH conditions on all airway surfaces were set to 37 °C and 99% to mimic the thermodynamic conditions *in vivo*. At the outlets of the TB airways, outflow boundary conditions were employed based on estimates of ventilation to each lung lobe. The following ventilation distribution estimates for each of the five lung lobes were chosen based on reported values in the literature (66, 67): right upper 14%, right middle 7%, right lower 33%, left upper 15%, left lower 31%. These lobar ventilation approximations resulted in a heterogeneous lung ventilation with right and left ventilation proportions of 54% and 46%, respectively.

Particle Formulation and Injections—The particles were injected as a polydisperse bolus of 9,000 discrete elements for this study. For EEG delivery, solid particles composed of 50:50 drug (AS): excipient (NaCl) based on mass were used. The hygroscopic parameter, which quantifies the hygroscopicity (44), was 77.9 kmol/m^3 for NaCl and 4.9 kmol/m^3 for AS, respectively. This parameter indicates that NaCl has much greater growth potential compared with AS. For the calculation of initial particle profiles and post-processing particle output files, FORTRAN routines were implemented.

Deposition Metrics—The fate of individual droplets is reported as either a deposition fraction (DF), deposition efficiency (DE), lung penetration fraction (PF) or fraction exhaled (FE). DF for i^{th} region is based on the nebulized dose as

$$DF_i = \frac{drug\ mass\ deposited\ in\ region\ i}{drug\ mass\ released\ from\ nebulizer} \times 100\,\% \quad (1)$$

In contrast, DE for i^{th} region is calculated as a percentage of drug mass that enters a region and deposits within that region

$$DE_i = \frac{drug\ mass\ deposited\ in\ region\ i}{drug\ mass\ entering\ region\ i} \times 100\,\% \quad (2)$$

The lung PF is the percentage of initial drug mass that enters the lung (approximated as the filter dose), and is calculated as

$$PF = \frac{drug\ mass\ collected\ at\ the\ filter}{drug\ mass\ released\ from\ nebulizer} \times 100\,\% \quad (3)$$

The FE from the nostrils is the percentage of initial drug mass that exits the nostrils during the time when the inhalation flow rate is less than the cannula flow rate

$$FE = \frac{drug\ mass\ exits\ the\ nostrils}{drug\ mass\ released\ from\ nebulizer} \times 100\,\% \quad (4)$$

In the NMT-TB CFD model, fraction remaining (FR) values at the lobe entrances were calculated for each lobe i as a percentage of nebulized drug mass reaching that lobe

$$FR_i = \frac{drug\ mass\ collected\ at\ the\ lobe\ i}{drug\ mass\ released\ from\ nebulizer} \times 100\,\% \quad (5)$$

CFD Validation Case Studies

Compared with the previously published CFD studies on condensational growth aerosol delivery from our group (13, 23, 49, 50, 53), the current CFD methods have been modified significantly, including polyhedral meshes (Figure 3), improved near-wall turbulence/velocity corrections and corresponding changes in the droplet growth codes, and fully parallelized UDFs. Hence, the CFD methods have been validated for multiple test cases by comparing with relevant experimental data either obtained from this study or using previously published data (23, 51).

The first validation test case was chosen as the condensational growth of submicrometer particles in a coiled tube geometry (51). This case is designed to provide residence times and thermodynamic conditions consistent with the lung airways, and it is one of the simplest geometries to illustrate the theory behind the controlled hygroscopic growth of aerosol. As implemented in the previous study of Longest et al. (51), the diameter of the coiled tube is approximately 22 mm and a sufficient length is implemented to provide a residence time

of 2.4 s. The geometry was held at 37°C and the tube wall was pre-wetted to provide a 100% RH surface condition. Aerosol sources for this experimental test case were a modified Respimat inhaler or a capillary aerosol generator, and the droplet size at the tube outlet was measured using cascade impaction. Additional details of this test case are provided in Longest et al. (51).

In addition to the coiled tube geometry, CFD predictions of deposition in the nasal cannula and NMT model were based on the previous *in vitro* data of Golshahi et al. (23) for conventional sized aerosols under a steady-state flow rate of 30 LPM. The last validation test case was the use of *in vitro* data from this study for synchronized EEG aerosol delivery from the small-volume mixer-heater with deep nasal inhalation. A preliminary simulation of the mixer-heater provided the parameters (i.e., timing delay) to design the *in vitro* experiments for synchronizing aerosol delivery. The deposition fractions and lung dose predicted using the transient CFD model were compared with the corresponding experimental data.

RESULTS

Experimental Data

Based on the CFD-predicted aerosol delay of ~0.2 s in the mixer-heater (as discussed in a subsequent section), an experimental study was conducted in which the nebulizer was activated ~ 0.1 after the start of inhalation and as a result aerosol reached the cannula tube ~0.3 s after the start of inhalation. Administering the aerosol with this timing ensures that the aerosol delivery is correctly synchronized, i.e., the aerosol reaches the cannula tube only when inhalation flow is greater than HFNC flow. The experimental data for particle sizing and deposition with a 0.1 s delay are presented in Table 1. The droplet size of the AS:NaCl aerosol exiting the drug nebulizer was experimentally determined to have a mean (SD) MMAD of 5.3 (0.1) μm, and after passing through the mixer-heater the measured mean (SD) MMAD was found to be 1.2 (0.1) μm. The mean (SD) total deposition in the mixer-heater device including nebulizer skirt, mixer-heater and Tubing 1 was 5.1% (3.9%) based on nebulized drug mass. Further, the mean (SD) deposition fractions in the cannula interface (Tubing 2 + cannula) and the NMT model were 7.1% (1.3%) and 4.2 (0.5%) based on nebulized dose, respectively. The overall mean (SD) drug recovery at the tracheal filter was 81.1% (7.3%) of the nebulized dose.

Grid Convergence

Grid convergence was determined using the grid convergence index (GCI) method, which was described by Roache (67) and based on Richardson extrapolation (68), as well as with comparisons to experimental *in vitro* data. In the current study, GCI was applied to the volume-averaged velocity magnitude (<Vmag>) and volume-averaged turbulent kinetic energy (<k>). Furthermore, regional depositions in a nasal cannula and nose model were compared with corresponding *in vitro* experimental data (23) to verify grid independence for the particle depositions. Three meshes of the cannula and nasal geometry with total cell counts of 1.4 M (Coarse), 2.8 M (Medium) and 4.9 M (Fine), respectively, were evaluated to determine the GCI values and deposition fractions for each of the meshes. As observed in Table 2, the absolute error in the total DF between the CFD predictions for the fine mesh

and corresponding experimental data was only 1.3% (the relative error was ~7%); whereas absolute errors in total DF prediction using medium and coarse meshes were 4.6% and 19.6%, respectively. Therefore, deposition fractions (DFs) predicted by the fine mesh best match the experimental data. The GCI values for <Vmag> and <k> when comparing the medium and fine grids were only ~0.5 and 3%, respectively. Based on these observations, the fine mesh was deemed acceptable and used in all subsequent simulations.

CFD Model Validation

Validation of the Evaporation/Condensation Codes using Coiled Tube Geometry—The CFD-predicted aerosol size change in a coiled tube geometry was validated with the previously reported *in vitro* data from our group (51). The final diameters predicted by CFD and corresponding *in vitro* data for budesonide:NaCl EEG particles (initial MMAD=0.75) with one-way and two-way coupling are presented in Figure 4a. As observed in the figure, the inclusion of two-way coupling provides an excellent match (2.49 μm) with the *in vitro* data (2.51±0.22 μm) for hygroscopic growth, while the one-way coupled solution slightly over-predicts the growth (3.25 μm). Nevertheless, considering the high computational cost required to simulate two-way coupling, one-way coupled solutions were viewed as reasonably accurate. Moreover, the larger droplet growth values predicted by the one-way coupled model will result in a conservatively high estimate of nasal deposition as a result of hygroscopic growth.

Validation of NMT Deposition for Steady-State Flow—Improved UDFs along with the new meshing strategy and the boundary conditions for the cannula/NMT geometry were further validated by comparing CFD-predicted depositions with *in vitro* experimental data of Golshahi et al. (23). The *in vitro* experimental conditions employed a 30 LPM flow rate from a HFNC gas source, aerosol generation from an Aeroneb Lab vibrating mesh nebulizer with a standard T-connection, a 0.1% AS:0.1%MN w/v in deionized water formulation, and a streamlined nasal cannula interface. The experimentally measured MMAD of the aerosol at the cannula outlet was 2.9 μm. The airway model was also held at 37°C with wetted airway walls. The CFD simulations modeled these experimental conditions as closely as possible, but assumed a monodisperse aerosol droplet size of 3.6 μm at the entry to the cannula inlet tube since experimentally measured droplet size was not available at that position. Golshahi et al. (23) found that to account for some droplet evaporation in the cannula and the monodisperse assumption of the polydisperse aerosol, the droplet size assumption of 3.6 μm at the entry to the cannula inlet tube was needed to match the experimentally measured aerosol size exiting the nasal cannula (2.9 μm). As shown in Figure 4b, the NMT DF predicted by CFD was 6.2%, a 1% absolute difference from the experimental value of 7.2%. The CFD-predicted cannula interface DF was 15.9% compared to the experimental value of 14.6% (1.3% absolute difference). Considering that the CFD model used a monodisperse aerosol size assumption at the tube inlet to simulate the experimentally measured polydisperse size distribution at the cannula outlet, the CFD-predicted depositions showed reasonable agreement with the experimental data.

Validation of NMT Deposition for Transient Flow with Synchronized Delivery—For validating the transient CFD model for synchronized EEG aerosol delivery with a deep

nasal inhalation, a concurrent *in vitro* experimental study was conducted. Planning the *in vitro* study with synchronized aerosol delivery required an understanding of the time spread and delay of the aerosol bolus as it travels from the drug nebulizer to the patient interface through the mixer-heater. Hence, a transient CFD simulation of drug aerosol transport in the small-volume mixer-heater was conducted. Previously, it was reported that for accurate prediction of deposition in the mixer-heater, a two-way coupled solution was required (13), which is extremely time-intensive. However, the purpose of the simulation in this study was to capture only the average spread and delay of the tracer drug particles, such that a one-way coupled solution could be employed. Figure 5 illustrates CFD simulation results for the transport of particles in the mixer-heater from a 1.5 s square wave particle injection. In Figure 5, the initial pulse of aerosol generation at the drug nebulizer is shown as a dashed line. The solid line represents the time course of aerosol through the outlet and illustrates that there is only a 0.2 s transit time within the mixer-heater and that the 1.5 s injected bolus has expanded by only ~ 0.1 s. Hence, transport through the mixer-heater is very rapid with minimal bolus spread.

A comparison of the CFD-predicted DF and PF in the cannula and NMT model (System 2) and the corresponding *in vitro* values are presented in Figure 6. Considering the complexities in CFD modeling, including transient inhalation, aerosol condensation and evaporation along with simplified assumptions such as one-way coupling and neglecting exhalation, excellent agreement was achieved between CFD predictions and corresponding *in vitro* data across multiple regions. The maximum absolute error in predicted regional DFs was 0.7% and absolute error in predicted PF was also 0.7%. The one-way coupled solutions for both steady-state (Figure 4b) and transient (Figure 6) flow in NMT showed excellent agreement with the *in vitro* data in terms of regional deposition fractions, which gives confidence in the CFD methods employed in this study for predicting nose-to-lung delivery through the trachea using hygroscopic aerosols.

Effect of Synchronizing EEG Aerosol Delivery with Deep Nasal Inhalation

Two cases of incorrectly or unsynchronized delivery scenarios (Unsync 1 and Unsync 2) were simulated using transient CFD and compared with correctly synchronized (Sync) delivery as shown in Table 3. These two incorrectly or unsynchronized cases were planned based on observations from the experimental studies with the mixer-heater feedback system for various randomized deep nasal inhalation profiles. As described previously, the drug nebulizer is actuated 0.1 s after the start of inhalation in the correctly synchronized case (Sync). Hence, the aerosol reaches the cannula tube inlet at ~0.3 s and lasts through 1.8 s (1.5 s nebulization). In the first unsynchronized case, Unsync 1, the aerosol at the cannula tube inlet is delivered at 0.1 s until 1.6 s, hence, a portion of the aerosol exits the nostrils due to an inhalation flow rate that is lower than the HFNC flow. The other unsynchronized case, Unsync 2, delays the start of aerosol injection (at the cannula inlet) to 0.75 s and continues delivering until 2.25 s, which is close to the end of inhalation. As indicated in Table 3, the DF values for cannula interface and NMT model have only small differences among the different synchronization cases. However, due to the potential for aerosol loss through the nose, lung dose (PF) values differ more substantially among the synchronization cases. Considering the PF values, Table 3 illustrates that the Sync case delivers 81.8% of the

nebulized drug mass to the filter; in contrast, Unsync 1 and Unsync 2 cases deliver 78.9% and 75.6%, respectively. Comparing FE between synchronized and unsynchronized cases it can be observed that only 0.1% of the drug mass exits through the nostrils for the Sync case compared to 3.1% and 3.9% for Unsync 1 and Unsync 2 cases, respectively.

Figure 7a presents the deposition fraction fate of aerosol groups injected at different time points (0.1 s bins) based on transient CFD simulations against the backdrop of the inhalation waveform. For example, aerosol injected into the cannula inlet tube at 0.5 s has a DF in the interface and NMT of approximately 8% and 5%, respectively. Surprisingly, both interface and NMT DF values remain flat across the time period. Figure 7b presents the transient behavior of PF and FE. Overall, the Sync case minimizes the FE and maximizes PF. Based on Figures 7a and 7b, it is evident from that the aerosol delivery to the cannula during 0.4 s to 1.7 s provides optimal delivery characteristics.

Comparison of EEG and Control Particles for Optimized Delivery

To evaluate the effectiveness of EEG delivery as compared to conventional aerosol delivery, a CFD-based comparison was made between the two approaches for a 1 s synchronized delivery as presented in Table 4. For CFD simulation of the conventional aerosol, the MMAD measured at the nebulizer exit (5.3 μm) was used. Based on Table 4, 55.3% of nebulized drug deposits in the cannula interface in the control case compared to 7.6% with EEG delivery. Further, conventional delivery incurs much higher depositional losses in the NMT model with a DE of 37.9% compared to 5.1% in the case of EEG delivery. Both conventional and EEG delivery provide very small FE because of correct delivery synchronization. Most importantly, EEG delivery provides a lung PF of 82.2% as compared to 27.5% with conventional nebulized delivery.

Comparison of NMT Deposition for Steady-State and Transient CFD Simulations

To avoid the complexity and computational expense of conducting transient CFD simulations of nose-to-lung aerosol delivery with a nasal cannula interface, it would be convenient to identify a representative steady state flow rate that efficiently captures the transient deposition. Table 5 compares deposition fractions between a fully transient CFD simulation and running steady-state CFD simulations with three methods to select a representative steady flow value: (i) time-averaged mean inhalation flow rate (Q_{mean}), (ii) peak flow rate (Q_{peak}), and (iii) effective flow rate using an average of mean and peak flow rate (Q_{eff}). The peak flow rate of the prescribed sinusoidal inhalation waveform was ~66 LPM and corresponding mean effective flow rates were 42 LPM and 54 LPM, respectively.

As shown in Table 5, it is observed that the cannula interface DF is always higher in the steady-state simulation as compared to transient simulation. However, the steady-state CFD-predicted NMT DF is smaller than the corresponding data from the transient simulation. It is observed that a steady-state simulation conducted at the waveform peak flow rate best matched the transient case in terms of predicting the NMT DF (absolute error of 0.5%) and the cannula interface DF (absolute error of 0.6%). Therefore, for studying the effect of inhalation flow rate on the deposition and transport of EEG aerosols in the NMT-TB model, steady-state runs were performed at peak waveform flow rates for multiple waveforms.

Effect of Flow Rate on Particle Deposition and Transport in NMT-TB Model

A representative model of the upper TB airways through approximately the lobar bifurcation [Model D from Walenga et al.(68)] was attached to the NMT geometry larynx to better predict lung delivery of the aerosol (Figure 8). Regional DFs, NMT DE and FE at different flow rates are presented in Figure 9. NMT DE is presented separately to highlight deposition in this region without the influence of FE and cannula DF. Overall, the DFs have little variation with the flow rate due to small particle sizes and co-flow arrangement. It is evident that at a nasal inhalation flow rate (Q) of 15 LPM, which is half of the HFNC flow rate, the deposition in the cannula, NMT and upper TB regions is very small; however, ~45% of the drug mass exits through the nostrils (represented as FE). When Q equals the HFNC flow rate (30 LPM), no flow exits the nostrils and the NMT DF is increased slightly compared to the Q = 15 LPM case. For Q larger than the HFNC flow rate, co-flow from the nostrils into the nose occurs, which helps to breakdown the recirculation zone in the NMT/cannula interface. Hence, increasing co-flow (by increasing Q) maintains a relatively constant nasal DF and DE. Nasal DE does not start to appreciably increase until approximately 90 LPM. A slight increase in upper TB deposition is observed as the Q increases from 30 through 90 LPM. Based on these observations, a range of targeted peak flow rate can be established between 40 LPM (peak flow rate when average flow rate is 30 LPM) to 75 LPM. The associated average flow rate range assuming a sinusoidal waveform is then ~30 LPM to 50 LPM. However, it is noted that peak flow rate can increase to as high as 90 LPM with <10% depositional loss in the NMT model.

Figure 10 illustrates the particle deposition locations for Q =30 LPM and Q=75 LPM contoured based on droplet size. It is observed that Q=75 LPM produces more particle deposition in the laryngeal region compared to Q =30 LPM, but co-flow reduces the deposition in the anterior portion of the nose. Overall, NMT DF for Q=75 LPM is 5.3% and Q=30 LPM is 6.0%.

The fraction of the nebulized drug entering each lobe entrance (lobe FR) and the total lobe FR values are presented in Figure 11 along with the representative air ventilation rates. Overall, particle transport to different lobes qualitatively follows the prescribed ventilation rates for the small size aerosol considered. It is observed that the Q = 40 to 75 LPM (target flow rate range) keeps the total FR close to 78% for all cases.

DISCUSSION

A major outcome of this study was to provide optimal aerosol administration and inhalation conditions for future human experiments of nose-to-lung aerosol delivery using the EEG approach during HFNC administration. CFD results demonstrated that while correct synchronization with inhalation does not have a significant effect on nasal deposition efficiency, small inaccuracies in nebulizer actuation timing (0.2 s too early or 0.5 s too late) begin to influence the dose delivered to the lungs. Further, CFD simulations showed that the inhalation flow rate does not have a significant effect on regional drug deposition and lung dose due to the combined effects of small-sized EEG particles and co-flow from the nostrils. The primary aim of this study was to achieve a lung delivery efficiency of 80% during cyclic breathing. For particles injected into the cannula tube inlet, the CFD-predicted lung delivery

efficiency with correct synchronization was 81.8%, which was confirmed by the realistic *in vitro* experimental study (81.1%). The targeted lung dose of 80% was achieved, yet, there are still opportunities for further improvements.

The CFD simulation of the mixer-heater demonstrated that due to its design, a 1.5 s drug aerosol bolus at the nebulizer was only expanded to ~1.6 s at the exit of the mixer-heater. Furthermore, nebulized aerosol crossed the mixer-heater within ~0.2 s, which can largely be attributed to the small volume of the mixer-heater device, which is around 100 ml (13). For synchronized aerosol delivery, the inhalation flow rate should be greater than the HFNC flow rate, thereby minimizing the potential for aerosol escape through the nostrils. For the deep nasal inhalation profile considered in this study, the inhalation flow rate rises above the HFNC flow rate at around 0.3 s and then falls again below the HFNC flow rate around 2.2 s. Therefore, synchronization in the experimental study could be achieved by delaying the nebulization 0.1 s after the start of inhalation, resulting in the aerosol reaching the patient at a time when the inhalation flow rate is approximately equal to the HFNC flow rate.

CFD results from the correctly synchronized case were compared with two incorrectly or unsynchronized cases, namely Unsync 1 and Unsync 2, respectively. Recall that for a 2.5 s inhalation with 1.5 s nebulization, the Sync case corresponds to aerosol delivery to the patient from 0.3 s to 1.8 s. In comparison to the Sync case, the Unsync 1 case delivers aerosols early in the inhalation phase (0.1–1.6 s) whereas, Unsync 2 delivers late in the inhalation cycle (0.75–2.25 s). CFD simulations reveal that both cannula interface and NMT DFs do not largely change with the aerosol delivery timing. Deposition in the cannula is a constant due to a constant flow rate of 30 LPM consistent with HFNC therapy, except for a small variation associated with deposition on the outer cannula walls. For the NMT region, constant DFs for different delivery timing windows are counterintuitive. Detailed CFD data on time-dependent behavior of particle fates for different injection times (Figure 7) revealed that NMT DF did not largely change if the aerosol was delivered when the inhalation flow rate was greater than HFNC flow rate. This behavior of flow rate independent DF in the NMT region can be attributed to small particle size and the effect of co-flow gas streams through the nostrils.

Comparing the CFD predicted lung dose between different transient cases showed that Sync provides the maximum lung dose of 81.8%, while Unsync 1 and Unsync 2 deliver 78.9% and 75.6%, respectively. Reduction in lung dose due to incorrect synchronization can be attributed to an increase in fraction exhaled through nostrils when the HFNC flow rate is greater than the inhalation flow rate. In case Unsync 2, further reduction in lung dose was observed due to a fraction of the drug still dispersed in the domain at the end of inhalation. CFD predicted transient distribution of particle fate (Figure 7) showed the limits where incorrect timing starts to impact lung delivery efficiency. Considering the high sensitivity to timing synchronization that was observed, it is recommended that the nebulization period be reduced to 1 s and that the aerosol is delivered to the cannula tube at ~0.4 s, i.e., time delay between the start of inhalation and start of nebulization should be increased to ~0.2 s, assuming a deep nasal inhalation profile during the time period of drug delivery.

Based on the synchronization study findings, transient CFD simulations compared delivery of EEG and conventional nebulized aerosols for synchronized delivery with a 1 s nebulization and aerosol delivery window (at the cannula tube inlet) of 0.4 s to 1.4 s. Overall, the EEG approach provides a three-fold increase in the lung delivered dose (82.2%) compared to conventional delivery (27.5%) due to the smaller size of the EEG aerosols. The predicted PF for conventional sized aerosol showed very good agreement with a previous steady-state CFD study on EEG during HFNC (53) (using conventional 5 μm particles with a streamlined cannula in an identical NMT model), where PF was reported as 28.3%. Furthermore, a recent *in vitro* study on HFNC by Bennett et al. (69) reported lung dose in the range of 20.6% to 30.1% for adults with a breathing rate of 15 breaths/minute with different spontaneous breathing patterns. There are a few notable differences in their setup (69), namely, tidal volumes were much smaller than the tidal volumes considered in this study, a larger HFNC flow rate of 50 LPM (compared to 30 LPM in this study), and a different nasal model. Nevertheless, CFD predicted lung dose (27.5%) for conventional sized aerosols agrees with their *in vitro* data (20.6%−30.1%).

Steady-state CFD simulations demonstrated that the deposition fractions, especially in the NMT region, do not vary significantly with an increase in the inhaled flow rate. Deposition in the NMT geometry showed only a slight increase even at flow rates as high as 90 LPM. This is a surprising result since it is well known that the flow rate strongly affects nasal deposition (70–72). This observation of constant NMT DF at different flow rates could be attributed to a combination of small particle size and co-flow through the nostrils. Small particle size limits the inertial parameter, $MMAD^2*Q$ ($\mu m^2 L/min$), to around 100 for the maximum flow rate of 90 LPM. Moreover, visualization of CFD results revealed that the co-flow entering from the nostrils breaks down a recirculation region near the interface and prevents depositional losses near the nostrils and in the entrance to the nasal cavity. As the co-flow increases, the deposition in these regions is reduced; however, a higher flow rate induces more deposition in the larynx region keeping overall NMT deposition constant. Walenga et al. (53) observed that the addition of 15 LPM co-flow to a 30 LPM HFNC gas improved PF for nose-to-lung delivery with small particles (~1 μm), while no improvement was observed with conventional sized aerosols (5 μm and larger). Although nasal deposition does not largely vary with the inhaled flow rate, CFD results demonstrated that an optimal peak waveform range of 40 LPM to 75 LPM should be targeted. This peak waveform range corresponds to a time-averaged (mean) flow rate range of ~30 LPM to 50 LPM. While higher flows produced only a marginal increase in NMT deposition, it is unlikely that flows higher than approximately 60 LPM would occur through the nose, even with HFNC assistance.

Limitations of this study include the use of one-way coupled simulations in most cases and a limited number of aerosol timing conditions. Although a one-way coupled solution over-predicts the growth as shown in Figure 4a, the CFD predicted deposition and PF values agree well with the corresponding *in vitro* experimental data for both steady and transient simulations (Figures 4b and 6). Considering timing of aerosol delivery, only two synchronization error cases were considered with relatively small errors. These conditions were selected to test the bounds of inhalation timing and resulted in relatively small decreases in lung delivered dose. Clearly larger synchronization errors would drastically

reduce the lung delivered dose. Furthermore, only one inhalation waveform was considered. Faster inhalation times will make dose synchronization more difficult. As a result, reducing the drug aerosol nebulization time to 1 s and potentially implementing a variable nebulization time are recommended.

In conclusion, the results of this study quantify the effects of aerosol delivery synchronization and inhaled flow rates on the regional deposition and lung delivery efficiencies for EEG aerosol delivery through a nasal interface. Transient CFD simulations of the small-volume mixer-heater show that due to its small volume the aerosol bolus has minimal spread and reaches the cannula with a time delay of only 0.2 s. Due to a combined effect of small particle sizes and co-flow arrangement, increasing the inhaled flow rate does not appreciably increase the nasal deposition even at flow rates as high as 90 LPM.

ACKNOWLEDGEMENTS

Research reported in this publication was supported by the National Heart, Lung and Blood Institute of the National Institutes of Health under Award Number R01HL107333. The content is solely the responsibility of the authors and does not necessarily represent the official views of the National Institutes of Health.

ABBREVIATIONS

ACI	Andersen Cascade Impactor
AS	Albuterol sulfate
CFD	Computational Fluid Dynamics
DE	Deposition efficiency
DF	Deposition fraction
EEG	Excipient enhanced growth
FE	Fraction exhaled
GCI	Grid convergence index
HFNC	High flow nasal cannula
HPLC	High performance liquid chromatography
LPM	Liters per minute
LRN	Low Reynolds number
MMAD	Mass median aerodynamic diameter
NaCl	sodium chloride
NIV	Non-invasive ventilation
NMT	Nose-mouth-throat
PF	Penetration fraction

RANS	Reynolds averaged Navier-Stokes
RH	Relative humidity
TB	Tracheobronchial
UDF	User defined function

REFERENCES

1. Bhashyam AR, Wolf MT, Marcinkowski AL, Saville A, Thomas K, Carcillo JA, and Corcoran TE. Aerosol delivery through nasal cannulas: An in vitro study. Journal of Aerosol Medicine and Pulmonary Drug Delivery. 2008;21:181–187. [PubMed: 18518794]
2. Longest PW, Golshahi L, Behara SRB, Tian G, Farkas DR, and Hindle M. Efficient nose-to-lung (N2L) aerosol delivery with a dry powder inhaler. Journal of Aerosol Medicine and Pulmonary Drug Delivery. 2015;28:189–201. [PubMed: 25192072]
3. Farkas D, Hindle M, and Longest PW. Application of an inline dry powder inhaler to deliver high dose pharmaceutical aerosols during low flow nasal cannula therapy. International journal of pharmaceutics. 2018;546:1–9. [PubMed: 29733972]
4. Hess DR. Aerosol therapy during noninvasive ventilation or high-flow nasal cannula. Respiratory Care. 2015;60:880–893. [PubMed: 26070581]
5. Dhand R Aerosol therapy in patients receiving noninvasive positive pressure ventilation. Journal of Aerosol Medicine and Pulmonary Drug Delivery. 2012;25:63–78. [PubMed: 22191396]
6. Farkas D, Hindle M, and Longest PW. Application of an inline dry powder inhaler to deliver high dose pharmaceutical aerosols during low flow nasal cannula therapy. International Journal of Pharmaceutics. 2018;10.1016/j.ijpharm.2018.05.011
7. Rubin BK. Pediatric aerosol therapy: New devices and new drugs. Respiratory Care. 2011;56:1411–1421. [PubMed: 21944688]
8. Laube BL. Aerosolized medications for gene and peptide therapy. Respiratory Care. 2015;60:806–824. [PubMed: 26070576]
9. Dixon AE. Rhinosinusitis and asthma: the missing link. Current Opinion in Pulmonary Medicine. 2009;15:19–24. [PubMed: 19077701]
10. Aanæs K Bacterial sinusitis can be a focus for initial lung colonisation and chronic lung infection in patients with cystic fibrosis. Journal of Cystic Fibrosis. 2013;12:S1–S20. [PubMed: 24064077]
11. Zeman KL, Rojas Balcazar J, Fuller F, Donn KH, Boucher RC, Bennett WD, and Donaldson SH. A trans-nasal aerosol delivery device for efficient pulmonary deposition. Journal of Aerosol Medicine and Pulmonary Drug Delivery. 2017;30:223–229. [PubMed: 28157412]
12. Geller DE. Aerosol antibiotics in cystic fibrosis. Respiratory Care. 2009;54:658–670. [PubMed: 19393109]
13. Spence BM, Longest PW, Wei X, Dhapare S, and Hindle M. Development of a high flow nasal cannula (HFNC) and pharmaceutical aerosol combination device. Journal of Aerosol Medicine and Pulmonary Drug Delivery. 2019;DOI: 10.1089/jamp.2018.1488
14. Rubin BK, and Fink JB. Aerosol therapy for children. Respir Care Clin N Am. 2001;7:175–213. [PubMed: 11517020]
15. Devadason SG. Recent advances in aerosol therapy for children with asthma. Journal of Aerosol Medicine-Deposition Clearance and Effects in the Lung. 2006;19:61–66.
16. Perry SA, Kesser KC, Geller DE, Selhorst DM, Rendle JK, and Hertzog JH. Influences of Cannula Size and Flow Rate on Aerosol Drug Delivery Through the Vapotherm Humidified High-Flow Nasal Cannula System. Pediatric Critical Care Medicine. 2013;14:E250–E256. [PubMed: 23628834]
17. Bennett G, Joyce M, Sweeney L, and MacLoughlin R. In Vitro Determination of the Main Effects in the Design of High-Flow Nasal Therapy Systems with Respect to Aerosol Performance. Pulmonary Therapy. 2018;10.1007/s41030-018-0054-x:1–14. [PubMed: 32026244]

18. DiBlasi RM. Clinical controversies in aerosol therapy for infants and children. Respiratory Care. 2015;60:894–916. [PubMed: 26070582]
19. Ward JJ. High-flow oxygen administration by nasal cannula for adult and perinatal patients. Respiratory Care. 2013;58:98–120. [PubMed: 23271822]
20. Nishimura M High-flow nasal cannula oxygen therapy in adults. Journal of Intensive Care. 2015;3:15. [PubMed: 25866645]
21. Dysart K, Miller TL, Wolfson MR, and Shaffer TH. Research in high flow therapy: Mechanisms of action. Respiratory Medicine. 2009;103:1400–1405. [PubMed: 19467849]
22. Golshahi L, Longest PW, Azimi M, Syed A, and Hindle M. Intermittent aerosol delivery to the lungs during high flow nasal cannula therapy. Respiratory Care. 2014;59:1476–1486. [PubMed: 24917454]
23. Golshahi L, Tian G, Azimi M, Son Y-J, Walenga RL, Longest PW, and Hindle M. The use of condensational growth methods for efficient drug delivery to the lungs during noninvasive ventilation high flow therapy. Pharmaceutical Research. 2013;30:2917–2930. [PubMed: 23801087]
24. Reminiac F, Vecellio L, Heuze-Vourc'h N, Petitcollin A, Respaud R, Cabrera M, Le Pennec D, Diot P, and Ehrmann S. Aerosol therapy in adults receiving high flow nasal cannula oxygen therapy. Journal of Aerosol Medicine and Pulmonary Drug Delivery. 2016;doi:10.1089/jamp.2015.1219
25. Dailey PA, Harwood R, Walsh K, Fink JB, Thayer T, Gagnon G, and Ari A. Aerosol delivery through adult high flow nasal cannula with heliox and oxygen. Respiratory Care. 2018;62:1186–1192.
26. Hess DR. The mask of noninvasive ventilation: Principles of design and effects on aerosol delivery. Journal of Aerosol Medicine. 2007;20:S85–S99. [PubMed: 17411410]
27. Dhand R Inhalation therapy in invasive and noninvasive mechanical ventilation. Current Opinion in Critical Care. 2007;13:27–38. [PubMed: 17198046]
28. Ari A, and Fink JB. Inhalation therapy in patients receiving mechanical ventilation: an update. Journal of Aerosol Medicine and Pulmonary Drug Delivery. 2012;25:319–332. [PubMed: 22856594]
29. Dugernier J, Hesse M, Jumetz T, Bialais E, Roeseler J, Depoortere V, Michotte J-B, Wittebole X, Ehrmann S, and Laterre P-F. Aerosol delivery with two nebulizers through high-flow nasal cannula: A randomized cross-over single-photon emission computed tomography study. Journal of Aerosol Medicine and Pulmonary Drug Delivery. 2017;30:349–358. [PubMed: 28463044]
30. Bräunlich J, and Wirtz H. Oral versus nasal high-flow bronchodilator inhalation in chronic obstructive pulmonary disease. Journal of Aerosol Medicine and Pulmonary Drug Delivery. 2018;31:248–254. [PubMed: 29261402]
31. Borgstrom L, Olsson B, and Thorsson L. Degree of throat deposition can explain the variability in lung deposition of inhaled drugs. Journal of Aerosol Medicine. 2006;19:473–483. [PubMed: 17196076]
32. Walenga RL, Longest PW, Kaviratna A, and Hindle M. Aerosol drug delivery during noninvasive positive pressure ventilation: Effects of intersubject variability and excipient enhanced growth. Journal of Aerosol Medicine and Pulmonary Drug Delivery. 2017;30:190–205. [PubMed: 28075194]
33. Weers J Inhaled antimicrobial therapy - Barriers to effective treatment. Advanced Drug Delivery Reviews. 2015;85:24–43. [PubMed: 25193067]
34. Barnes PJ. New anti-inflammatory targets for chronic obstructive pulmonary disease. Nature Reviews Drug Discovery. 2013;12:543–559. [PubMed: 23977698]
35. Barnes PJ. Development of new drugs for COPD. Current Medicinal Chemistry. 2013;20:1531–1540. [PubMed: 22963554]
36. Longest PW, Walenga RL, Son Y-J, and Hindle M. High efficiency generation and delivery of aerosols through nasal cannula during noninvasive ventilation. Journal of Aerosol Medicine and Pulmonary Drug Delivery. 2013;26:266–279. [PubMed: 23273243]

37. Longest PW, Golshahi L, and Hindle M. Improving pharmaceutical aerosol delivery during noninvasive ventilation: Effects of streamlined components. Annals of Biomedical Engineering. 2013;41:1217–1232. [PubMed: 23423706]
38. Longest PW, and Hindle M. Systems, devices, and methods for changing therapeutic aeorsol size and improving efficiency of ventilation and aerosol drug delivery. US Patent 10,010,692 B2. 2018;
39. Golshahi L, Walenga RL, Longest PW, and Hindle M. Development of a transient flow aersol mixer-heater system for lung delivery of nasally administered aerosols using a nasal cannula. Aerosol Science and Technology. 2014;48:1009–1021.
40. Schuster J, Rubsamen R, Lloyd P, and Lloyd J. The AERx™ aerosol delivery system. Pharmaceutical Research. 1997;14:354–357. [PubMed: 9098880]
41. Denyer J, Nikander K, and Smith N. Adaptive aerosol delivery (AAD®) technology. Expert Opin. Drug Deliv 2004;1:165–176. [PubMed: 16296727]
42. Longest PW, and Hindle M. Improved delivery of submicrometer and nanometer aerosols to the lungs using hygroscopic excipients or dual stream nasal delivery. US Patent No. 9,433,588 B2. 2016;
43. Longest PW, Hindle M, and Xi J. Enhanced delivery of nano- and micro-sized pharmaceutical aerosols through controlled hygroscopic growth. US Patent 8,479,728. 2013;
44. Longest PW, and Hindle M. Numerical model to characterize the size increase of combination drug and hygroscopic excipient nanoparticle aerosols. Aerosol Science and Technology. 2011;45:884–899. [PubMed: 21804683]
45. Hindle M, and Longest PW. Condensational growth of combination drug-excipient submicrometer particles for targeted high efficiency pulmonary delivery: Evaluation of formulation and delivery device. Journal of Pharmacy and Pharmacology. 2012;64:1254–1263. [PubMed: 22881438]
46. Hindle M, and Longest PW. Evaluation of enhanced condensational growth (ECG) for controlled respiratory drug delivery in a mouth-throat and upper tracheobronchial model. Pharmaceutical Research. 2010;27:1800–1811. [PubMed: 20454837]
47. Longest PW, Tian G, Li X, Son Y-J, and Hindle M. Performance of combination drug and hygroscopic excipient submicrometer particles from a softmist inhaler in a characteristic model of the airways. Annals of Biomedical Engineering. 2012;40:2596–2610. [PubMed: 22820981]
48. Son Y-J, Longest PW, Tian G, and Hindle M. Evaluation and modification of commercial dry powder inhalers for the aerosolization of submicrometer excipient enhanced growth (EEG) formulation. European Journal of Pharmaceutical Sciences. 2013;49:390–399. [PubMed: 23608613]
49. Tian G, Hindle M, and Longest PW. Targeted lung delivery of nasally administered aerosols. Aerosol Science and Technology. 2014;48:434–449. [PubMed: 24932058]
50. Tian G, Longest PW, Li X, and Hindle M. Targeting aerosol deposition to and within the lung airways using excipient enhanced growth. Journal of Aerosol Medicine and Pulmonary Drug Delivery. 2013;26:248–265. [PubMed: 23286828]
51. Longest PW, and Hindle M. Condensational growth of combination drug-excipient submicrometer particles: Comparison of CFD predictions with experimental results. Pharmaceutical Research. 2012;29:707–721. [PubMed: 21948458]
52. Kim CS, and Jaques PA. Respiratory dose of inhaled ultrafine particles in healthy adults. Philosophical Transactions Of The Royal Society Of London Series A-Mathematical Physical And Engineering Sciences. 2000;358:2693–2705.
53. Walenga RL, Tian G, Hindle M, Yelverton J, Dodson K, and Longest PW. Variability in nose-to-lung aerosol delivery. Journal of Aerosol Science. 2014;78:11–29. [PubMed: 25308992]
54. Longest PW, Tian G, and Hindle M. Improving the lung delivery of nasally administered aerosols during noninvasive ventilation - An application of enhanced condensational growth (ECG). Journal of Aerosol Medicine and Pulmonary Drug Delivery. 2011;24:103–118, DOI: 10.1089/jamp.2010.0849. [PubMed: 21410327]
55. Franca EET, de Andrade AFD, Cabral G, Almeida P, Silva KC, Galindo VC, Marinho PEM, Lemos A, and Parreira VF. Nebulization associated with Bi-level noninvasive ventilation: Analysis of pulmonary radioaerosol deposition. Resp Med. 2006;100:721–728.

56. ICRP. Human Respiratory Tract Model for Radiological Protection, Elsevier Science Ltd., New York, 1994.
57. Delvadia RR, Longest PW, Hindle M, and Byron PR. In Vitro Tests for Aerosol Deposition. III: Effect of Inhaler insertion angle on aerosol deposition. Journal of Aerosol Medicine and Pulmonary Drug Delivery. 2013;26:145–156. [PubMed: 23025452]
58. Longest PW, Hindle M, Das Choudhuri S, and Byron PR. Numerical simulations of capillary aerosol generation: CFD model development and comparisons with experimental data. Aerosol Science and Technology. 2007;41:952–973.
59. Longest PW, and Xi J. Condensational growth may contribute to the enhanced deposition of cigarette smoke particles in the upper respiratory tract. Aerosol Science and Technology. 2008;42:579–602.
60. Gosman AD, and Ioannides E. Aspects of computer simulation of liquid-fueled combustors. Journal of Energy. 1981;7:482–490.
61. Matida EA, Finlay WH, and Grgic LB. Improved numerical simulation of aerosol deposition in an idealized mouth-throat. Journal of Aerosol Science. 2004;35:1–19.
62. Wang Y, and James PW. On the effect of anisotropy on the turbulent dispersion and deposition of small particles. International Journal of Multiphase Flow. 1999;22:551–558.
63. Longest PW, and Xi J. Effectiveness of direct Lagrangian tracking models for simulating nanoparticle deposition in the upper airways. Aerosol Science and Technology. 2007;41:380–397.
64. Longest PW, Kleinstreuer C, and Buchanan JR. Efficient computation of micro-particle dynamics including wall effects. Computers & Fluids. 2004;33:577–601.
65. Bass K, and Longest PW. Recommendations for simulating microparticle deposition at conditions similar to the upper airways with two-equation turbulence models. Journal of Aerosol Science. 2018;10.1016/j.jaerosci.2018.02.007
66. Horsfield K, Dart G, Olson DE, and Cumming G. Models of the human bronchial tree. Journal of Applied Physiology. 1971;31:207–217. [PubMed: 5558242]
67. Asgharian B, and Price OT. Airflow distribution in the human lung and its influence on particle deposition. Inhalation Toxicology. 2006;18:795–801. [PubMed: 16774869]
68. Walenga RL, Tian G, and Longest PW. Development of characteristic upper tracheobronchial airway models for testing pharmaceutical aerosol delivery. ASME Journal of Biomechanical Engineering. 2013;135(9):091010.
69. Bennett G, Joyce M, Sweeney L, and MacLoughlin R. In vitro study of the effect of breathing pattern on aerosol delivery during high-flow nasal therapy. Pulmonary Therapy. 2019;5:43–54. [PubMed: 32026423]
70. Kelly JT, Asgharian B, Kimbell JS, and Wong B. Particle deposition in human nasal airway replicas manufactured by different methods. Part I: Inertial regime particles. Aerosol Science and Technology. 2004;38:1063–1071.
71. Cheng YS. Aerosol deposition in the extrathoracic region. Aerosol Science and Technology. 2003;37:659–671. [PubMed: 19011693]
72. Golshahi L, Noga ML, Thompson RB, and Finlay WH. In vitro deposition measurement of inhaled micrometer-sized particle in extrathoracic airways of children and adolescents during nose breathing. Journal of Aerosol Science. 2011;42:474–488.

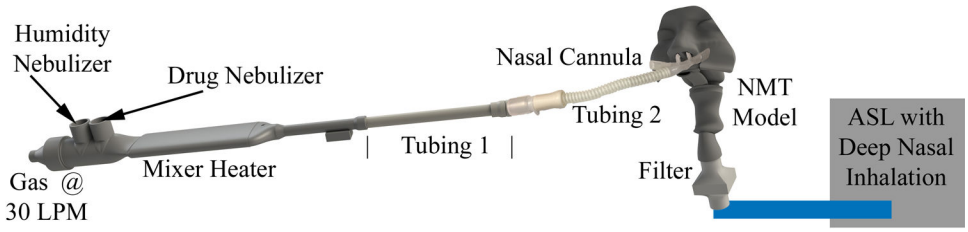

Figure 1.

Schematic of the *in vitro* experimental set-up showing the mixer-heater, nasal cannula interface, and the nose-mouth-throat (NMT) model

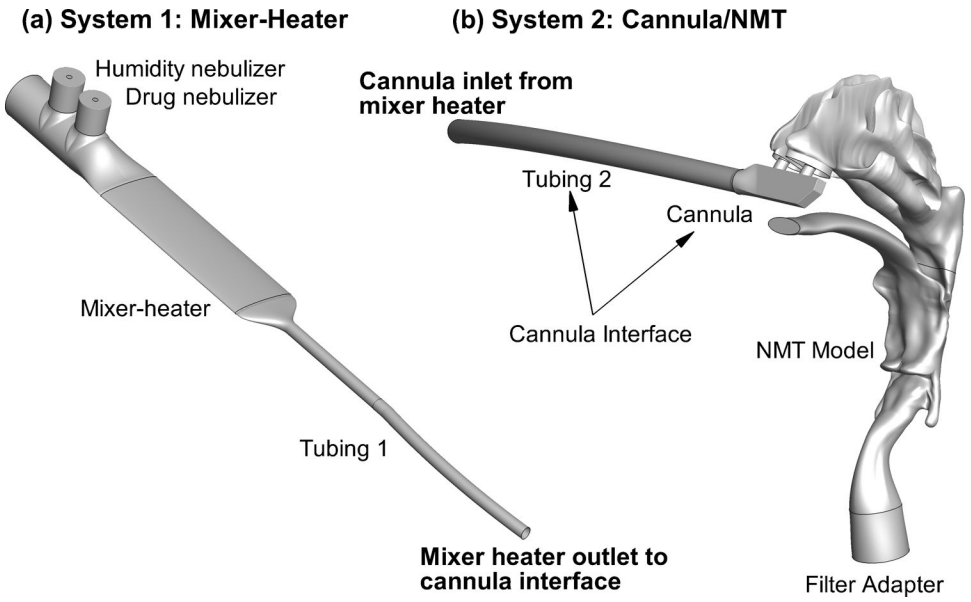

Figure 2.

CFD model geometries divided as System 1: Mixer-Heater and System 2: Cannula /NMT. System 1 consists of nebulizers, mixer-heater and Tubing 1. System 2 consists of cannula interface (Tubing 2 +nasal cannula) and NMT Model

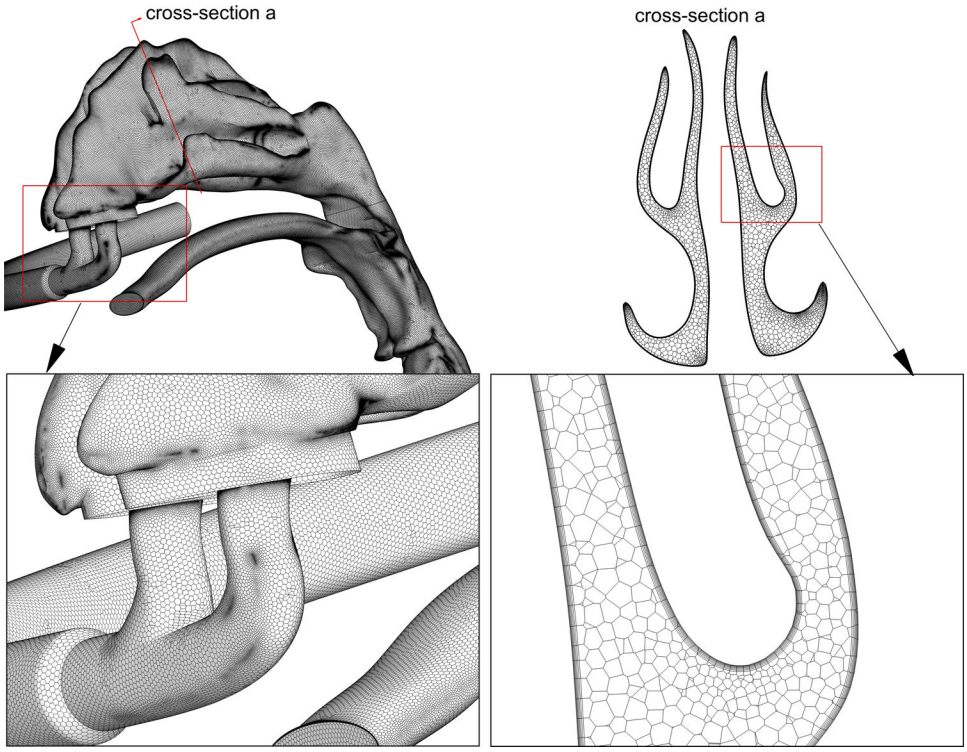

Figure 3.
Polyhedral meshing of the cannula interface/nose-mouth-throat (NMT) system depicting surface and volumes meshes

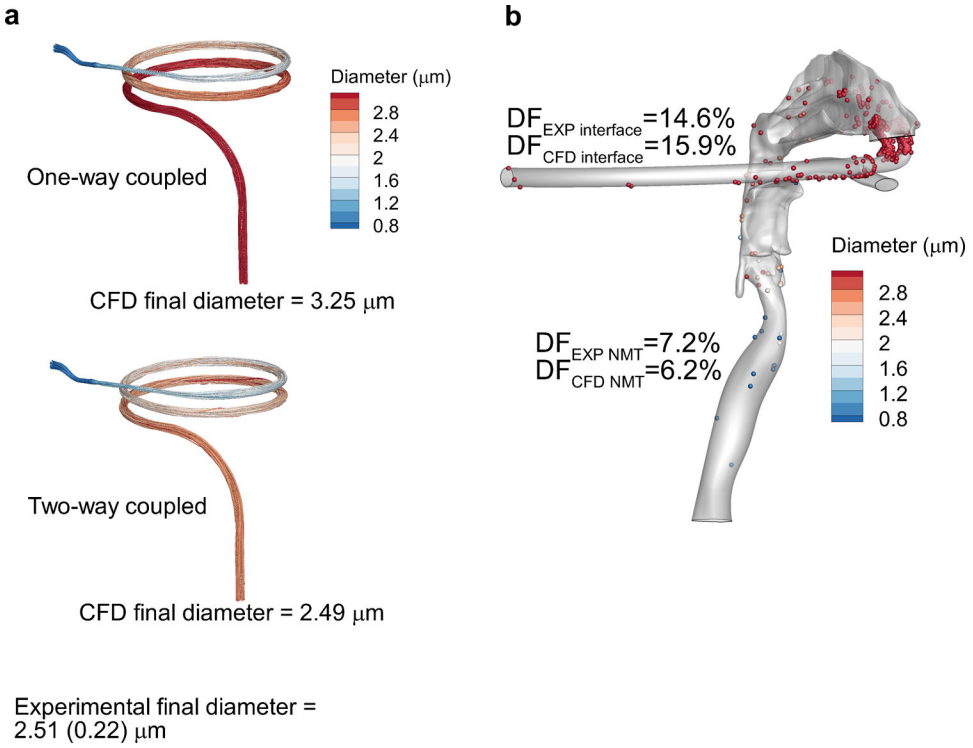

Figure 4.

CFD model validation cases including (a) droplets in a coiled tube geometry, (b) droplet deposition in cannula interface/nose-mouth-throat (NMT) system with HFNC under steady-state inhalation

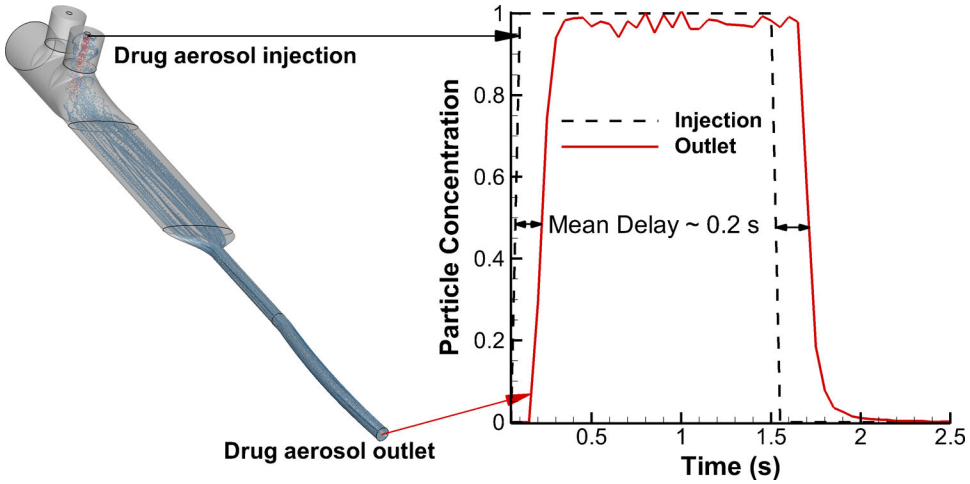

Figure 5.

CFD-predicted transient particle concentrations at the inlet and outlet of the mixer-heater at a mixer-heater flow rate of 30 LPM. Particle concentration for each time bin (0.05 s) is calculated as the number of particles (injected or at the outet)/number of injected particles

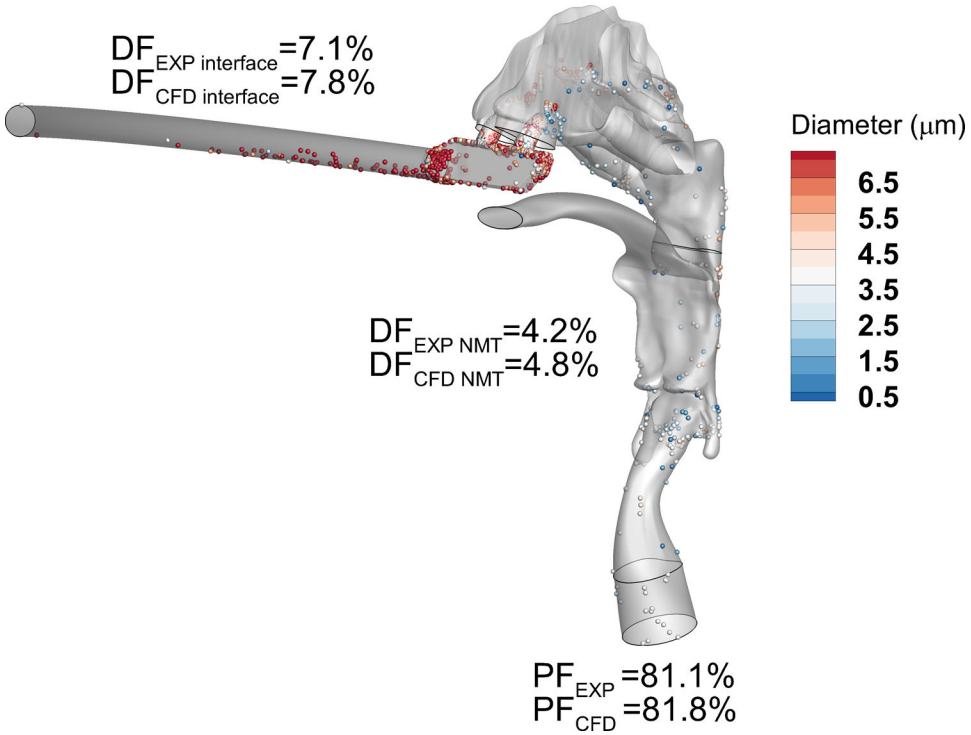

Figure 6.

CFD model validation case for droplet transport and deposition in cannula interface/nose-mouth-throat (NMT) system and HFNC under deep nasal inhalation

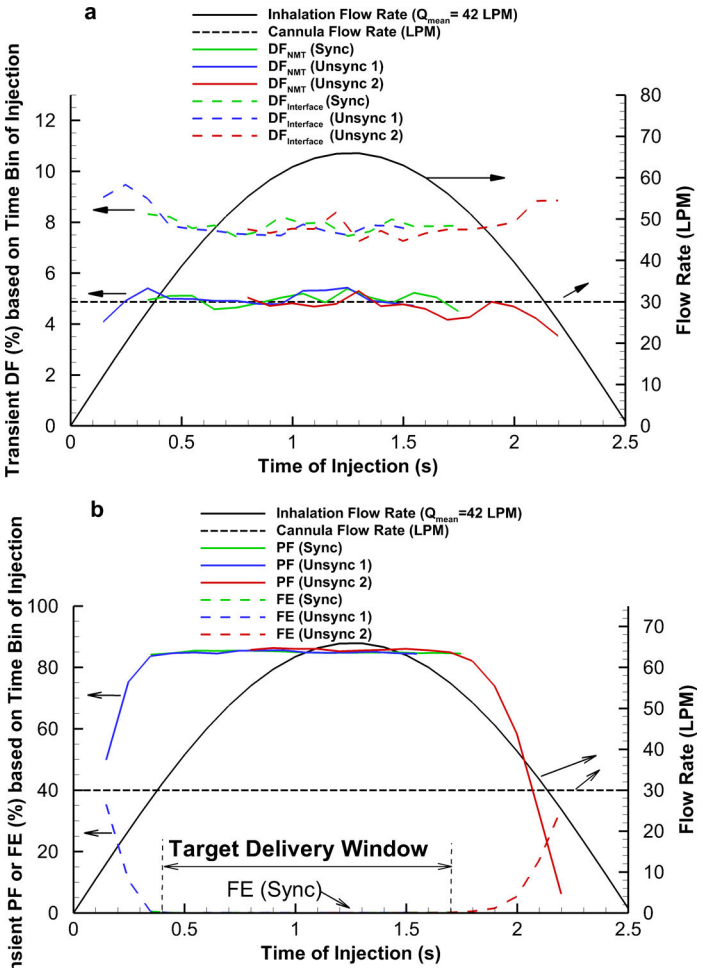

Figure 7.

The fate of the particles based on the time of injection for synchronized and unsynchronized cases: (a) transient deposition fraction (DF) (b) penetration fraction (PF) or fraction exhaled (FE)

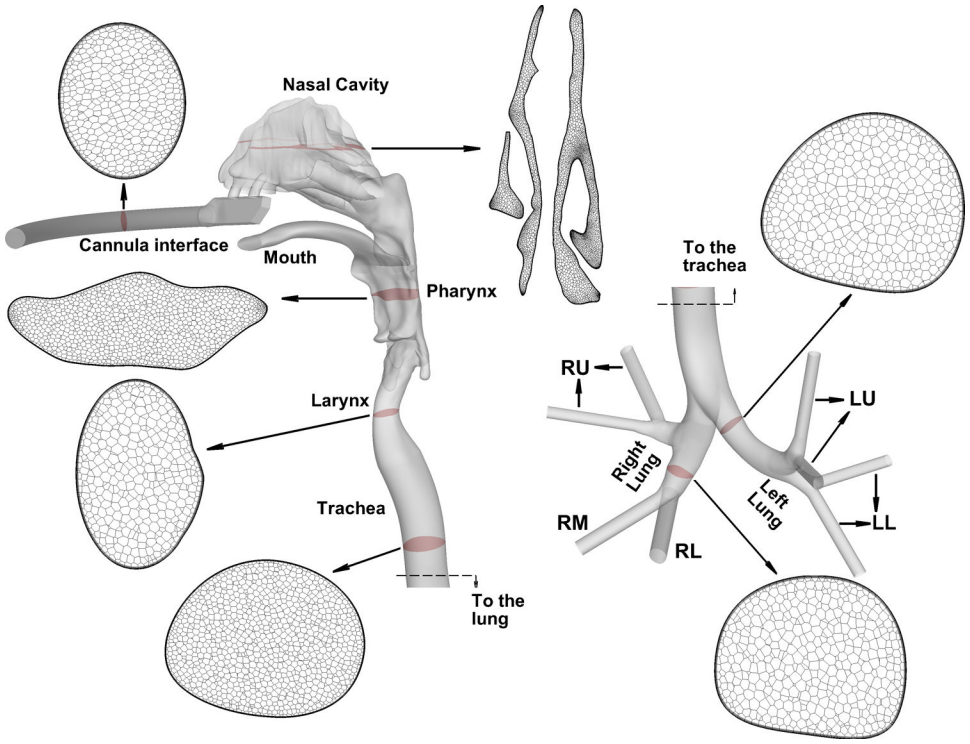

Figure 8.
Computational model of the NMT-TB geometry illustrating polyhedral meshing at various sections.

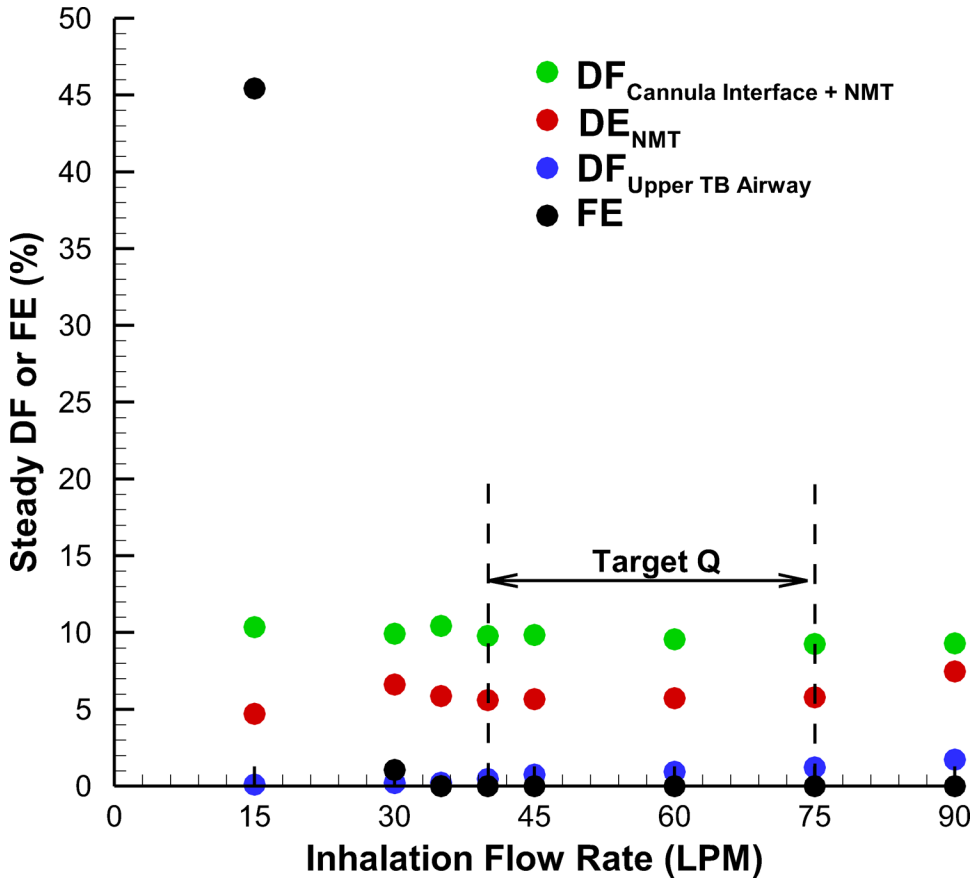

Figure 9.

CFD predictions for the effect of inhaled flow rates on the regional steady-state deposition fraction (DF), deposition efficiency (DE) and fraction exhaled (FE)

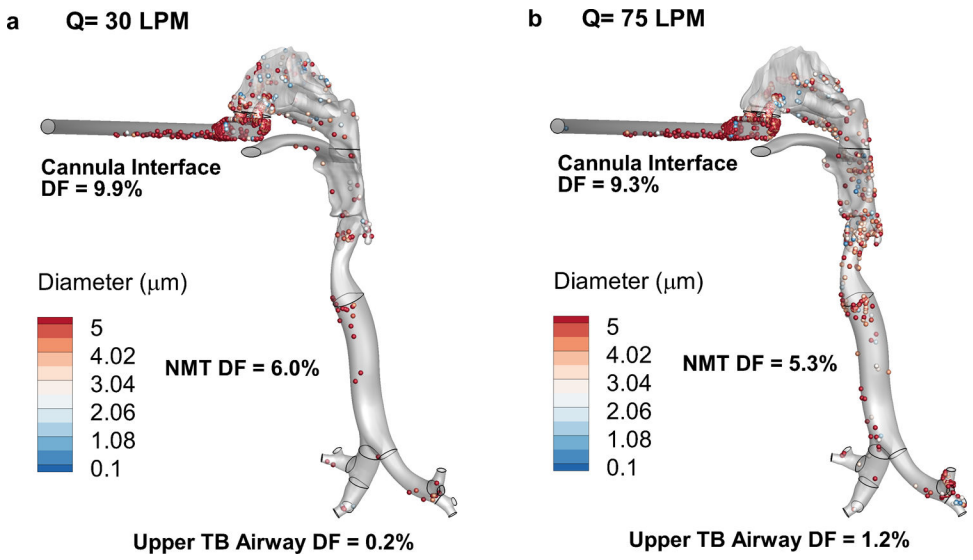

Figure 10.

Particle deposition locations at flow rates of (a) 30 LPM and (b) 75 LPM as predicted by CFD for the NMT-TB model with AS:NaCl EEG formulation

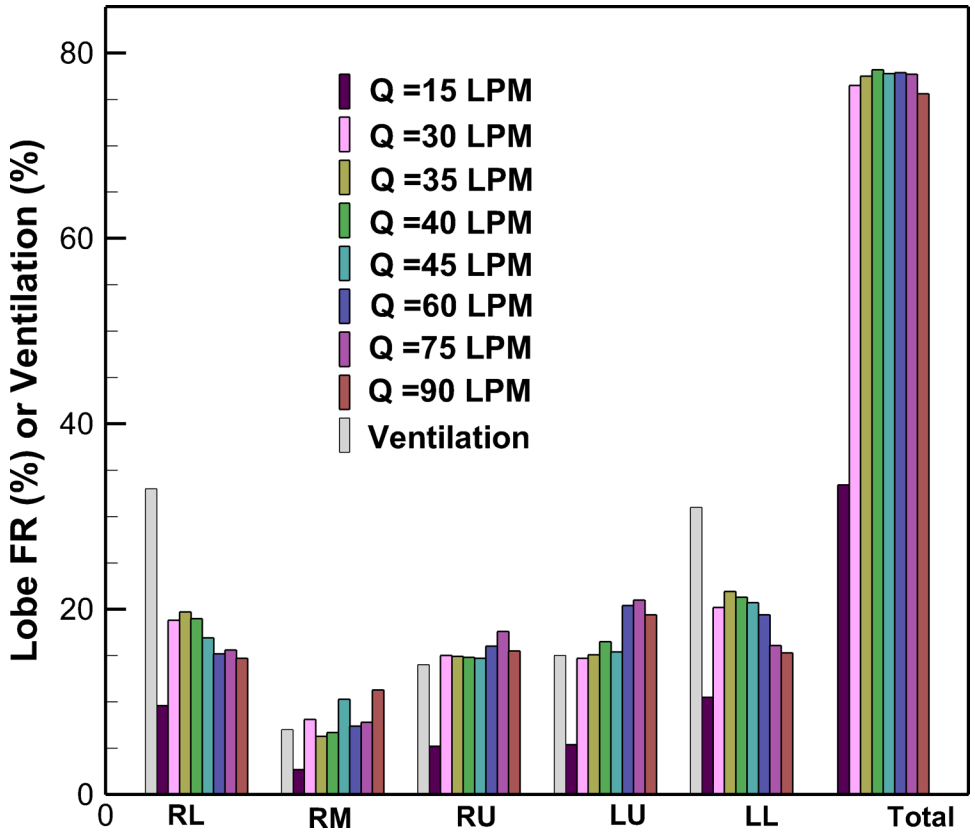

Figure 11.

CFD-predicted results for fraction remaining (FR) entering individual lobes and the total lobar FR under various inhaled flow rates. The assumed air fow ventilation entering each lung lobe is also provided for comparison.

Table 1.

In vitro experimental data for synchronized aerosol delivery with deep nasal inhalation profiles.[a]

Device DF (%)				Cannula Interface DF (%)			NMT Model DF (%)	Filter(%)	Drug Recovery (%)	MMAD (μm)	
Nebulizer	Mixer-Heater	Tubing 1	Total	Tubing 2	Nasal Cannula	Total				Nebulizer Exit	Mixer-Heater Exit
1.5	1.2	2.5	5.1 (±3.9)	1.7	5.5	7.1 (±1.3)	4.2 (±0.5)	81.1 (±7.3)	97.5 (±2.6)	5.3 (±0.1)	1.2 (±0.1)

[a]Deposition fractions and the filter recovery fractions are calculated based on nebulized drug mass

Table 2.

Comparison of DF values in different regions based on *In vitro* experiments [mean (SD)] and CFD simulations with three grid resolutions (Coarse, Medium, Fine).

	***In Vitro* Experiments**	**Coarse (1.4M) CFD**	**Medium (2.8M) CFD**	**Fine (4.9M) CFD**
Cannula Interface DF (%)	14.6 (±3.0)	27.6	19.25	15.9
NMT DF (%)	7.2 (±0.6)	12.8	6.12	6.2
Total DF (%)	20.8 (±3.6)	40.4	25.4	22.1
Absolute Error in Total DF (%)	-	19.6	4.6	1.3

Table 3.

Comparison of synchronized and unsynchronized delivery using transient CFD model.

Injection Type	Particle Injection Start Time at the Cannula Inlet Tube (s)	Particle Injection End Time at the Cannula Inlet Tube (s)	Cannula Interface DF (%)	NMT DF (%)	PF (%)	FE (%)
Sync	0.3	1.8	7.8	4.8	81.8	0.1
Unsync 1	0.1	1.6	8.0	4.6	78.9	3.1
Unsync 2	0.75	2.25	7.9	4.6	75.6	3.9

Table 4.

CFD-based comparison of EEG and control cases with optimized aerosol delivery.

	Particle Injection Start Time at the Cannula Inlet Tube (s)	Particle Injection End Time at the Cannula Inlet Tube (s)	Cannula Interface DF (%)	NMT DE (%)	PF (%)	FE (%)
Control (5.3 μm)	0.4	1.4	55.3	37.9	27.5	0.01
EEG (1.2 μm)	0.4	1.4	7.6	5.1	82.2	0.02

Table 5:

Comparison of predicted deposition fractions using transient and steady-state CFD solutions

	Transient DF	**Steady DF (Q_{mean} = 42 LPM)**	**Steady DF (Q_{eff} =54 LPM)**	**Steady DF (Q_{peak} = 66 LPM)[a]**
Cannula Interface	7.8	8.6	8.6	8.4
NMT	4.8	4.0	3.9	4.3

[a]Steady peak flow gave the best combined estimate of transient DF